Permanent Scatterers in SAR Interferometry

Alessandro Ferretti, Claudio Prati, and Fabio Rocca

Abstract—Temporal and geometrical decorrelation often prevents SAR interferometry from being an operational tool for surface deformation monitoring and topographic profile reconstruction. Moreover, atmospheric disturbances can strongly compromise the accuracy of the results. In this paper, we present a complete procedure for the identification and exploitation of stable natural reflectors or permanent scatterers (PSs) starting from long temporal series of interferometric SAR images. When, as it often happens, the dimension of the PS is smaller than the resolution cell, the coherence is good even for interferograms with baselines larger than the decorrelation one, and all the available images of the ESA ERS data set can be successfully exploited. On these pixels, submeter DEM accuracy and millimetric terrain motion detection can be achieved, since atmospheric phase screen (APS) contributions can be estimated and removed. Examples are then shown of small motion measurements, DEM refinement, and APS estimation and removal in the case of a sliding area in Ancona, Italy. ERS data have been used.

Index Terms—Differential interferometry, digital elevation model (DEM) reconstruction, geodetic measurements, radar data filtering, synthetic aperture radar (SAR).

I. INTRODUCTION

REPEAT-pass satellite SAR interferometry (InSAR) is potentially a unique tool for low cost precise digital elevation models (DEM) generation and large-coverage surface deformation monitoring [9], [12], [16], [17]. As is well known, the technique involves interferometric phase comparison of SAR images gathered at different times and with different baselines and has the potential to provide DEMs with meter accuracy and terrain deformations with millimetric accuracy [20]. In principle, DEMs and deformation patterns can be estimated on a very dense grid (4 × 20 m for ERS images) at low cost compared with any other traditional method.

Limitations are essentially due to temporal and geometrical decorrelation and atmospheric inhomogeneities. Temporal decorrelation [10] makes InSAR measurements unfeasible over vegetated areas and where the electromagnetic profiles and/or the positions of the scatterers change with time within the resolution cell. Geometrical decorrelation [10], [25] limits the number of image pairs suitable for interferometric applications and prevents one from fully exploiting the data set available. Atmospheric inhomogeneities create an atmospheric phase screen (APS) superimposed on each SAR image that can seriously compromise accurate deformation monitoring. In fact, the APS exhibits a low-wavenumber spectral behavior (according to the atmospheric water vapor distribution in the troposphere

[11], [8], [26], [24]) and cannot be detected and estimated from the coherence map associated with each interferogram [2].

The main goal of this paper is the identification of image pixels, hereafter called permanent scatterers (PSs), coherent over long time intervals [3], [4]. When, as it often happens, the dimension of the PS is smaller than the resolution cell, the coherence is good even for interferograms with baselines larger than the decorrelation one [6], and all the available images of the ERS data set can be successfully exploited for interferometric applications. On these pixels, submeter DEM accuracy and millimetric terrain motion detection can be achieved once APS contributions have been estimated and removed. It will be shown that even if no fringes can be seen generating single interferograms, reliable elevation and velocity measurements can be obtained on this subset of image pixels and can be used as a "natural" GPS network to monitor sliding areas [3] (as in the case presented in Section IV), urban subsidence [4], seismic faults, and volcanoes [7].

The use of sparsely populated phase data to estimate a geophysical signal of interest has lately gained increasing attention in differential SAR Interferometry (DInSAR) [21], [22], [34]. Here we use a multi-interferogram framework to identify highly coherent targets, to overcome most of the difficulties related to phase unwrapping and to better discern the different signals that concur to the interferometric phase. The starting point is a set of differential interferograms that use the same master acquisition. The DEM used for differential interferograms generation can be either a topographic profile estimated from the Tandem pairs of the ERS data set, or an *a priori* DEM already available. Its accuracy is not a real constraint (20 m is enough). In fact, as already mentioned, DEM refinement (in correspondence to the PS) is one of the products of the processing presented in the following sections. Even though we consider a constant velocity model for targets motion (i.e., we estimate just the local velocity field of the area under study in correspondence of the PS grid), this constraint can be relaxed using a more complex processing [4] but using essentially the same framework. Moreover, a uniform strain rate hypothesis is often used in geophysical modeling, e.g., seismic faults motion, urban subsidence, lava compaction, etc.

The aim of the paper is to make a step further toward an operational use of DInSAR data for civil protection purposes and a fully exploitation of the huge data set already acquired by the ESA ERS satellites.

II. PHASE CHANGE IN REPEAT-PASS SAR INTERFEROMETRY

Although the theory of SAR interferometry has already been presented in some detail in several papers [25], [9], [12], [15], [6], in this section, we review the main results to establish notation and to highlight the different physical signals that con-

tribute to the interferometric phase. For the sake of simplicity, phase terms due to thermal noise, image misregistration, wrong focusing parameters, etc. will be neglected [27]. The analysis outlines the rationale behind a multi-image approach to DEM generation and surface displacements estimation.

It is well known that a pixel in a SAR image changes its phase due to: 1) satellite-scatterer relative position; 2) possible temporal changes of the target; and 3) atmospheric variations (APS). Considering $K + 1$ SAR images of the same area, the phase of pixel $\underline{x} = [\begin{smallmatrix} \xi \\ \eta \end{smallmatrix}]$ (ξ and η being azimuth and slant range coordinates respectively) of the generic kth focused SAR image is thus the sum of different phase contributions

$$\psi_k(\underline{x}) = \frac{4\pi}{\lambda} r_k(\underline{x}) + \sigma_k(\underline{x}) + a_k(\underline{x}) \qquad (1)$$

where r is the satellite-target distance, σ is the scatterer reflectivity phase, and a is the atmospheric phase contribution. Let us now consider one of the $K + 1$ images as the reference "master" acquisition m. The phase difference of the generic "slave" image k with respect to the master one will be indicated with $\phi_k(\underline{x})$

$$\begin{aligned} \phi_k(\underline{x}) &= \psi_k(\underline{x}) - \psi_m(\underline{x}) \\ &= \frac{4\pi}{\lambda} [r_k(\underline{x}) - r_m(\underline{x})] + [\sigma_k(\underline{x}) - \sigma_m(\underline{x})] \\ &\quad + [a_k(\underline{x}) - a_m(\underline{x})] . \end{aligned} \qquad (2)$$

In repeat-pass interferometry, we can express r_k as follows:

$$r_k = r_m + \Delta r_k + \Delta \mu_k \qquad (3)$$

where Δr_k is the range variation due to the different satellite position, and $\Delta \mu_k$ is the possible target *motion* in the direction of the satellite line-of-sight (LOS), occurring during the time interval between the two acquisitions. The order of magnitude of the first contribution is usually tens or hundreds of meters, while the latter can be a millimetric surface deformation. The interferometric phase $\phi_k(\underline{x})$ is then a blend of several signals that depends on the acquisition geometry (satellite positions and topography), terrain motion, scattering changes (due to temporal variations and/or baseline decorrelation), and atmospheric inhomogeneities

$$\phi_k(\underline{x}) = \phi_{rk}(\underline{x}) + \phi_{\mu k}(\underline{x}) + \phi_{ak}(\underline{x}) + \phi_{\sigma k}(\underline{x}) \qquad (4)$$

where we posed

$$\begin{aligned} \phi_{rk}(\underline{x}) &= \frac{4\pi}{\lambda} \Delta r_k(\underline{x}) \\ \phi_{\mu k}(\underline{x}) &= \frac{4\pi}{\lambda} \Delta \mu_k(\underline{x}) \\ \phi_{ak}(\underline{x}) &= \frac{4\pi}{\lambda} (a_k(\underline{x}) - a_m(\underline{x}) \\ \phi_{\sigma k}(\underline{x}) &= \frac{4\pi}{\lambda} (\sigma_k(\underline{x}) - \sigma_m(\underline{x})) . \end{aligned} \qquad (5)$$

A. *DEM Estimation from Highly Coherent Interferograms*

We shall now discuss the problem of DEM estimation from the interferometric SAR phase referring to the ERS Tandem case. Let us begin with a single interferometric pair formed by a master m and a slave image k. Due to the short time interval between the images (one day), we can usually neglect terrain motion. The perpendicular baseline B_k between the slave and the master image is in general much smaller than the decorrelation one (about 1200 m [6]), and it is a function of both range and azimuth coordinate. The interferometric phase of (4) can then be approximated as follows

$$\begin{aligned} \phi_k(\underline{x}) &= \phi_{rk}(\underline{x}) + \phi_{ak}(\underline{x}) + \phi_{\sigma k}(\underline{x}) \\ &= \phi_{qk}(\underline{x}) + \phi_{\eta k}(\underline{x}) + \phi_{ak}(\underline{x}) + \phi_{\sigma k}(\underline{x}) . \end{aligned} \qquad (6)$$

In fact, we can split the geometrical term $\phi_{rk}(\underline{x})$ into two terms related to the elevation q and to the slant range position η of the scatterer as

$$\begin{aligned} \phi_{qk}(\underline{x}) &= \frac{4\pi}{\lambda R} B_k(\underline{x}) \frac{q(\underline{x})}{\sin \alpha} \\ \phi_{\eta k}(\underline{x}) &= \frac{4\pi}{\lambda R} B_k(\underline{x}) \frac{\eta}{\tan \alpha} \end{aligned} \qquad (7)$$

where R is the master sensor-target distance, and α is the local incidence angle with respect to the reference ellipsoid.

It is well known that the elevation $q(\underline{x})$ derived from the unwrapped phase $\phi_k(\underline{x})$ will be affected by baseline errors (smaller than 1 m in the case of ERS German precise orbits [30] and ERS orbital data processed by Delft University, Delft, The Netherlands [29]), decorrelation noise ($\phi_{\sigma k}$), and APS (ϕ_{ak}) [2]. The following elevation error expression holds

$$\begin{aligned} \Delta q(\underline{x}) &= \widehat{q}(\underline{x}) - q(\underline{x}) \simeq -q(\underline{x}) \frac{\Delta B_k(\underline{x})}{B_k(\underline{x})} \\ &\quad - \eta \cos \alpha \frac{\Delta B_k(\underline{x})}{B_k(\underline{x})} + \frac{\lambda R \sin \alpha}{4\pi B_k(\underline{x})} \\ &\quad \cdot (\phi_{\sigma k}(\underline{x}) + \phi_{ak}(\underline{x})) \end{aligned} \qquad (8)$$

where ΔB_k is the normal baseline error relative to image k

$$\Delta B_k(\underline{x}) = \widehat{B}_k(\underline{x}) - B_k(\underline{x}).$$

Using a baseline greater than 200 m and precise orbits, the ratio $\Delta B_k(\underline{x})/(B_k(\underline{x}))$ is usually less than 10^{-3}, so the first elevation error contribution in (8) is usually less than a few meters. On the contrary, the second term is a low order polynomial that can generate large systematic errors on wide areas. This contribution can be compensated either by using ground control points [23] or a reference low resolution DEM [2].

As far as the last term in (8) is concerned, $\phi_{\sigma k}(\underline{x})$ can be considered a random phase fluctuation with a power dependent on the local coherence (and it can be very high even in tandem interferograms on areas with dense vegetation), whereas $\phi_{ak}(\underline{x})$ is usually a low frequency phase distortion essentially due to the space inhomogeneities of the atmospheric water vapor concentration. The impact of these phase contributions depends on the normal baseline. In general, even with the highest tandem baselines, APS and noise can produce errors of tens of meters [2].

As recently proposed in [2] several tandem pairs can be exploited to reduce the elevation errors caused by atmospheric variations. Given K tandem interferograms, K DEMs of the same area can be generated. Each DEM will be affected by the elevation noise described by (8). These K DEMs can be averaged with weights dependent on 1) the normal baseline of each interferogram; 2) the mean square value of the APS estimated in different wavenumber bands; and 3) the estimated local coherence.

In [2], it is also shown that after optimum data combination, the elevation error is concentrated at very low wavenumbers due to residual atmospheric contributions and baseline errors [see (8)]. Thus, a fusion of a multi-interferogram DEM (at high wavenumbers) and a DEM obtained with different techniques characterized by elevated accuracy at low wavenumbers (e.g., stereo SPOT) allows one to get the best elevation accuracy.

As a conclusion, estimated DEM accuracy (5–6 m) is now limited by the largest available tandem baseline (< 500 m). The difficulties related to phase unwrapping of high-baseline interferograms can be overcome using multibaseline techniques [1], [5].

III. USING LARGE TEMPORAL AND GEOMETRICAL BASELINES

Following the framework presented in the previous section, we shall now discuss the use of large temporal and geometrical baselines starting from the problem of accurate DEM reconstruction. In fact, to further improve elevation accuracy with respect to the multitandem approach, more images and larger baselines should be exploited. However, it is well known that, as the baseline increases toward the critical value, only scatterers smaller than the resolution cell would allow reliable phase measurements [10], [6]. Moreover, ERS tandem pairs have generally small baselines and if larger ones are requested, larger time intervals between the acquisitions should be accepted. The latter condition (long temporal baselines) implies temporal stability of the targets and reduces their population. The former condition (pointwise scatterers) implies a further selection.

Similar considerations hold for differential applications for surface deformation monitoring. In particular, if the area of interest suffers from a secular time variation where the strain rate is uniform, high temporal baselines should be exploited for accurate estimation of the local velocity field in the direction of the LOS. Again, interferometric pairs with high temporal baselines and low geometrical baseline might be not available. Moreover, more interferograms should be used to reduce the impact of the APS on the estimated motion.

As a consequence, large baseline SAR interferometry can be carried out, fully exploiting the ERS data set, only on a *sparse distribution of pointwise stable scatterers* on the ground.

In the following, we shall consider $K + 1$ ERS SAR images taken on a large time interval (e.g., five to six years in the data set used in this work) and with baselines up to the decorrelation one with respect to a reference acquisition selected as the "master image" m. A novel technique that allows us to identify pointwise stable scatterers (PSs) and to accurately estimate their elevation and LOS velocity is now presented.

A. General Formulation of the Problem

Let us indicate with $\underline{\Phi}$ the $[K \times H]$ matrix of the interferometric phases $\phi_k(\underline{x})$ of H pixels considered PS candidates (selection of this subset of image pixel will be discussed later on). The kth row of $\underline{\Phi}$ contains the interferometric phases of image k with respect to the master image m of H pixels arbitrarily ordered with column index h

$$\underline{\Phi} = \underline{a}\mathbf{1}^T + \underline{p}_\xi\,\underline{\xi}^T + \underline{p}_\eta\,\underline{\eta}^T + \underline{B}\,\underline{q}^T + \underline{T}\,\underline{v}^T + \underline{E} \quad (9)$$

where

- $\underline{a}[K \times 1]$ are constant phase values;
- $\underline{p}_\xi\,[\mathbf{K} \times \mathbf{1}]$ and $\underline{p}_\eta\,[\mathbf{K} \times \mathbf{1}]$ contain the slope values of the linear phase components, along the azimuth $\underline{\xi}\,[H \times 1]$ and slant range $\underline{\eta}\,[H \times 1]$ direction, due to atmospheric phase contributions and orbital fringes;
- $\underline{B}[K \times 1]$ contains the normal baseline values (referred to the master image). For large areas, $\underline{B}$ cannot be considered constant, and the array $\underline{B}[K \times 1]$ may become a matrix $\underline{B}$ $[K \times H]$. However, for simplicity's sake, we shall use the previous simplified equation;
- $\underline{q}\,[H \times 1]$ contains the elevation of each PS times $4\pi/(\lambda R \sin \alpha)$;
- $\underline{T}\,[K \times 1]$ contains the time interval between the K slave images and the master;
- $\underline{v}[H \times 1]$ contains the slant range velocities of the PS's;
- $\underline{E}[K \times H]$ contains the residues that include atmospheric effects different from constant and linear components in azimuth and slant range, phase noise due to temporal and baseline decorrelation, and the effects of possible nonuniform pixel motion.

As formulated in (9), the problem would be linear if the unwrapped values of matrix phase $\underline{\Phi}$ were available. We have $H \cdot K$ equations and $3K + 2H$ unknowns: $\underline{a}$, $\underline{p}_\xi$, $\underline{p}_\eta$, $\underline{q}$, $\underline{v}$. Data are $\underline{\Phi}$, $\underline{\xi}$, $\underline{\eta}$, $\underline{B}$, $\underline{T}$. Thus, in principle, (9) could be inverted to get the local topography, the velocity field, and constant and linear phase contributions. In practice, however, we face a *nonlinear* system of equations (phase values are wrapped modulo 2π) to be solved by means of an iterative algorithm, and an available DEM (possibly obtained using the tandem pairs of the same data set) should be exploited to initialize the iterations. Moreover, PS candidate selection does not allow one to identify and exploit all the coherent targets in the area of interest. As will be shown, the H PS candidates are a good starting point to solve the nonlinear problem at hand. In fact, most of the PSs are actually identified after APS estimation and removal by means of a time series analysis of their phase values.

B. Zero-Baseline Steering

Our first goal is to rephase all K slave images k with respect to the master one in order to compensate for the geometric phase contribution $\phi_{rk}(\underline{x}) = \phi_{qk}(\underline{x}) + \phi_{sk}(\underline{x})$ [(5)] as if they were taken from the same master orbit (i.e., K differential interferograms are generated). Anyway, due to unavoidable orbit indeterminations and DEM errors, zero-baseline steering cannot be perfectly achieved.

The "topographic phase component" $\phi_{qk}(\underline{x})$ can be estimated from the satellite state vectors and the available DEM as

$$\widehat{\phi}_{qk}(\mathbf{x}) = \frac{4\pi}{\lambda R}\,\widehat{B_k}(\mathbf{x})\frac{\widehat{q}(\mathbf{x})}{\sin\,\alpha} \qquad (10)$$

where $\widehat{B_k}(\mathbf{x})$ is the estimated normal baseline and $\widehat{q}(\mathbf{x})$ is the available topography (i.e., its accuracy is generally around 10 m). The phase error of the topographic component has the following expression:

$$\phi_{qk}(\mathbf{x}) - \widehat{\phi}_{qk}(\mathbf{x})$$
$$= \frac{4\pi}{\lambda R \sin\,\alpha}\left[q(\mathbf{x})\cdot\Delta B_k(\mathbf{x}) + \widehat{B_k}(\mathbf{x})\cdot\Delta q(\mathbf{x})\right] \quad (11)$$

where $\Delta q(\mathbf{x}) = \widehat{q}(\mathbf{x}) - q(\mathbf{x})$ is the DEM error. As already discussed in the previous sections, the first term in (11) is very small and will be neglected. On the contrary, for large baseline $\widehat{B_k}$, the phase component proportional to the DEM error Δq can be relevant.

As far as $\phi_{sk}(\mathbf{x})$ is concerned, possible orbit indeterminations impact as follows:

$$\phi_{sk}(\mathbf{x}) - \widehat{\phi}_{sk}(\mathbf{x}) = \frac{4\pi}{\lambda R}\Delta B_k(\mathbf{x})\frac{\eta}{\tan\,\alpha}. \qquad (12)$$

If the area of interest is small (say 5×5 km) and precise orbits are used, this phase contribution can be well approximated by a linear phase component.

The estimated geometric phase contribution can then be subtracted from the interferometric phase $\underline{\Phi}$ in order to get a first estimate of the *zero baseline steered* interferometric phases

$$\underline{\Delta\Phi} = \underline{\mathbf{a}}\mathbf{1}^T + \underline{\mathbf{p}_\xi}\,\underline{\xi}^T + \underline{\mathbf{p}_\eta}\,\underline{\eta}^T + \underline{\mathbf{B}}\,\underline{\Delta q}^T + \underline{\mathbf{T}}\,\underline{\mathbf{v}}^T + \underline{\mathbf{E}} \quad (13)$$

where $\underline{\mathbf{p}_\xi}$ and $\underline{\mathbf{p}_\eta}$ now take into account, apart from the APS, the residual linear components of $\phi_{sk}(\mathbf{x}) - \widehat{\phi}_{sk}(\mathbf{x})$.

The nonlinear system 13 can be solved (and the unknowns $\underline{\mathbf{a}}$, $\underline{\mathbf{p}_\xi}$, $\underline{\mathbf{p}_\eta}$, $\underline{\Delta q}$, $\underline{\mathbf{v}}^T$ can then be estimated) provided that: 1) the SNR is high enough (i.e., the H selected pixels are only slightly affected by decorrelation noise); 2) the constant velocity model for target motion is valid; and 3) the APS can be approximated as a phase ramp. The last condition can be fulfilled (as a first order approximation) if the area of interest is small (say 5×5 km), while a uniform strain rate hypothesis is often used in geophysical modeling. More complex methods should be adopted when target motion in nonuniform [4]. The main problem is then to properly select the PS candidates (i.e., the H pixels).

C. PS Candidates Selection

In order to identify stable targets, the coherence maps associated with the interferograms could be exploited. Correlation thresholding would be the easiest approach. If a target exhibits a coherence always greater than a suitable value, that would be selected as a PS candidate. However, due to the high dispersion of the baseline values and the limited accuracy of the DEM, several coherence maps turn out to be useless. In fact, coherence computation implies space averaging of the data inside a suitable estimation window. If phase values are not properly compensated for, the topographic (and possibly the target motion) contribution, coherence, is underestimated. We can limit the analysis to

interferometric pairs with baseline smaller than 200–300 m, but the choice of the estimation window and the coherence threshold to be used for PS identification is not trivial at all.

The problem can be stated as follows. On the one hand, PS candidates (PSC) selection should be reliable (i.e., only a small percentage of selected pixels should be affected by decorrelation noise). On the other hand, the detection probability should be as high as possible (so that most of the PS can be effectively identified). The two variables to be optimized are the coherence threshold and the dimension of the estimation window. The larger the window dimension, the higher the estimator accuracy (low false-alarm rate), but the lower the resolution (low detection probability). In fact, using large estimation windows (i.e., averaging the data over large areas), many stable targets surrounded by noncoherent clutter are lost. Similar considerations hold for coherence thresholding. Window dimension and coherence threshold are then the result of a tradeoff between false-alarm rate and detection probability, a classical detection problem [19]. The result of this kind of approach is usually a set of a few disconnected *regions* (not single pixels) where several selected targets are actually affected by decorrelation noise.

Better results in terms of resolution can be achieved using a different strategy. Since we suppose that many SAR images (>30) are available, we can analyze the time series of the *amplitude* values of each pixel in the area of interest, looking for stable scatterers. In fact, while phase stability can be assessed only after estimation and removal of the different phase contributions, absolute values are almost insensitive to most of the phenomena that contribute to the phase values (APS, DEM errors, terrain deformation, orbit indeterminations, etc.). Since we are looking for targets slightly affected by geometrical and temporal decorrelation, pixels exhibiting a very "stable" sequence of amplitude values (in spite of the high temporal and geometrical baseline dispersion) should be selected as PSC.

More precisely, let us focus on a PS characterized by a complex reflectivity g. Without loss of generality, we suppose $\angle g = 0$ (i.e., g is a positive real number). We then consider a complex circular gaussian noise n characterized by a power σ_n^2 for both real (n_R) and imaginary components (n_I). The distribution of the amplitude values $\mathcal{A}_k$ is given by the Rice distribution [18]

$$f_\mathcal{A}(a) = \frac{a}{\sigma_n^2}I_0\left(\frac{ag}{\sigma_n^2}\right)e^{-(a^2+g^2)/2\sigma_n^2} \quad a > 0 \qquad (14)$$

where I_0 is the modified Bessel function. The shape of the Rice distribution depends on the SNR (i.e., the ratio g/σ_n). For low SNR, the Rice probability density function (PDF) tends to a Rayleigh distribution, which only depends on the noise variance σ_n^2, while at high SNR ($g/\sigma_n > 4$), $f_\mathcal{A}(a)$ approaches a Gauss distribution. In fact, provided that $\sigma_n \ll |g|$, the following equation holds:

$$\sigma_\mathcal{A} \simeq \sigma_{n_R} = \sigma_{n_I} \qquad (15)$$

since the modulus is primarily affected by the noise component parallel to $g(n_R)$. The *phase* dispersion (σ_ν) can then be estimated starting from the amplitude dispersion

$$\sigma_\nu \simeq \frac{\sigma_{n_I}}{g} \simeq \frac{\sigma_\mathcal{A}}{m_\mathcal{A}} \triangleq D_\mathcal{A} \qquad (16)$$
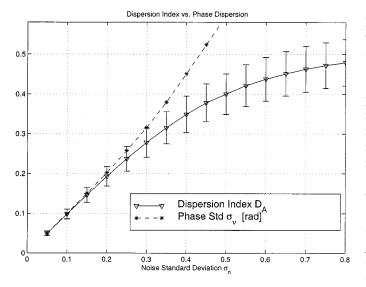
Fig. 1.   Numerical simulation results. Signal model: $z_i = g + n_i$ ($i = 1, \cdots, K + 1$). The value of g was fixed to 1, while the noise standard deviation (σ_n) was gradually incremented from 0.05 to 0.8. For each value of σ_n, 5000 estimates of the dispersion index of the amplitude values ($\mathcal{A} = |z|$) were carried out. 34 data were supposed to be available ($K = 33$). The mean values (solid line) and the dispersion (error bars) of the estimates $\widehat{D_{\mathcal{A}}}$ are reported, together with the values of the phase standard deviation (dotted line). Small values of $D_{\mathcal{A}}$ are good estimates of the phase dispersion.

where $m_{\mathcal{A}}$ and $\sigma_{\mathcal{A}}$ are the mean and the standard deviation of the amplitude values $\mathcal{A}_k$. The *dispersion index* $D_{\mathcal{A}}$ is then a measure of phase stability, at least for high SNR values. PSC can then be selected computing the dispersion index of the amplitude values relative to each pixel in the area of interest and considering only those targets exhibiting $D_{\mathcal{A}}$ values under a given threshold (typically $D_{\mathcal{A}} < 0.25$).

Although more rigorous and computationally intensive statistical analyses can be adopted (e.g., ML estimation of the parameters of the Rice distribution given the data), this very simple approach ($D_{\mathcal{A}}$ thresholding) turns out to be enough for our purposes. In fact, for PSC selection, we are interested in high SNR values only (low $D_{\mathcal{A}}$) and approximations 16 are valid. The processing to be carried out is then fast and effective, at least for a first selection of the targets. As will be shown, others PSs can be identified after APS removal by means of a time series analysis of the phase values.

The results of a numerical simulation reported in Fig. 1 (using 34 amplitude data, to be consistent with the data set used in the experimental section) highlight potentials and limits of such an approach. The value of g was fixed to 1, while noise standard deviation was gradually increased from 0.05 to 0.8. For each value of σ_n, 5000 estimates of the dispersion index $D_{\mathcal{A}}$ were carried out. The mean values (solid line) and the dispersion (error bars) of the estimates $\widehat{D_{\mathcal{A}}}$ are reported, together with the values of the phase standard deviation (dotted line). For low SNR, the dispersion index tends to the value proper for the Rayleigh distribution ($\sqrt{(4 - \pi)/\pi} \simeq 0.5$ [18]), while small values of $D_{\mathcal{A}}$ are good estimates of the phase dispersion.

It is important to point out that before statistical analysis of the amplitude values, images must be radiometrically corrected in order to make them comparable. Actually, since we are not interested in the backscattering coefficient σ^0, it suffices to com-

pensate the amplitude data for a suitable calibration factor $\mathcal{K}$, depending on the sensor (ERS-1 or ERS-2), the acquisition date and the processing center. Values for $\mathcal{K}$ are provided by ESA [13].

The advantages of this kind of approach are twofold: 1) fast processing and 2) no resolution loss. Of course, the accuracy is a function of the number of images available. A by product is the incoherent average of the SAR data ($m_{\mathcal{A}}$, multi-image reflectivity map), where the impact of speckle noise is strongly reduced and the spatial resolution of the image is preserved.

D. System Solution

After PSC selection, system 13 can be solved by means of an iterative algorithm (Appendix A). Basically, DEM errors $\Delta\mathbf{q}$ and velocities $\mathbf{v}$ are computed starting from small spatial and temporal baselines and improving their accuracy as soon as better estimation and removal of the linear phase terms have been carried out. Since the system is highly nonlinear, convergence is not guaranteed, depending on the following factors:

1) space-time distribution of the acquisitions (which should be as uniform as possible: spatial and/or temporal "holes" in the data set should be avoided);
2) reference DEM accuracy ($\Delta\mathbf{q}$ should generate small phase contributions for low $\overline{B_k}$);
3) dimensions of the area of interest (APSs and orbital fringes should be well approximated by linear phase components);
4) target motion should be slow enough to avoid aliasing and be well approximated by the constant velocity model. For convergence, $\mathbf{v}$ should generate small phase contributions for low T_k.

Results obtained with different test sites [3], [7] (one of which will be presented in the experimental section of this paper) have shown how constraints 1) and 2) are easily met using the ERS data set and a reference DEM obtained using the multitandem approach [2]. Larger areas and targets suffering nonuniform motion can be monitored using a more complex processing [4].

E. Atmospheric Phase Screen and Ensemble Coherence Estimation

As a result of the procedure described in the previous section, we get a precise estimation of DEM errors $\widehat{\Delta\mathbf{q}}$ and LOS velocities $\widehat{\mathbf{v}}$ of the PSC, together with constant and linear components of the APSs ($\widehat{\mathbf{a}}\,\widehat{\mathbf{p}_{\xi}}$ and $\widehat{\mathbf{p}}_{\eta}$). If the constant velocity model is valid, phase residues are due to atmospheric effects different from a phase ramp and phase noise (mostly due to temporal and baseline decorrelation)

$$\underline{\mathbf{E}'} = \left(\underline{\Delta\Phi} - \widehat{\underline{\Delta\Phi}}\right)$$
$$= \underline{\Delta\Phi} - \left(\widehat{\underline{\mathbf{a}}}\mathbf{1}^T + \widehat{\underline{\mathbf{p}}_{\xi}}\,\boldsymbol{\xi}^T + \widehat{\underline{\mathbf{p}}_{\eta}}\,\boldsymbol{\eta}^T + \underline{\mathbf{b}}\,\widehat{\underline{\Delta\mathbf{q}}}^T + \underline{\mathbf{T}}\,\widehat{\mathbf{v}}^T\right) \tag{17}$$
$$= \underline{\mathbf{E}'}_{atmo} + \underline{\mathbf{E}'}_{noise} \tag{18}$$

with obvious symbol meaning. In order to filter out $\underline{\mathbf{E}'}_{noise}$ and to estimate the atmospheric disturbances, we can take advan-

tage of the strong correlation of the atmospheric components at short distances, and we can smooth spatially the phase residues, taking into account the power spectrum of $\underline{\mathbf{E}}'_{atmo}$ [24]. Moreover, once the APSs have been estimated on the sparse grid (the H PS candidates), we can interpolate them on the uniform image grid. Both operations (filtering and resampling) can be performed at the same time using kriging interpolation [35].

The mean value of the estimated atmospheric components in the differential interferograms

$$\mathbf{APS}^T_{master} = \frac{1}{K} \left\{ \underline{\mathbf{1}}^T \cdot \widehat{\underline{\mathbf{E}'_{atmo}}} + (\widehat{\underline{\mathbf{a}}} \underline{\mathbf{1}}^T + \widehat{\underline{\mathbf{p}}}_\xi \, \underline{\boldsymbol{\xi}}^T + \widehat{\underline{\mathbf{p}}}_\eta \, \underline{\boldsymbol{\eta}}^T) \right\} \tag{19}$$

is an estimation of the atmospheric phase contribution relative to the master image. Its accuracy depends on the number of available images, the density of PSs, and the reliability of $\widehat{\underline{\Delta\Phi}}$. Once $\mathbf{APS}_{master}[H \times 1]$ has been computed, the APSs relative to each *single* SAR acquisition can be easily obtained by subtraction.

From these estimated quantities, the phase of each slave image can be modified as if it were taken from the master orbital position in absence of terrain motion and atmospheric effects. The new set of phases of the modified slave images will be indicated as

$$\underline{\boldsymbol{\zeta}} = \underline{\boldsymbol{\Psi}} - \left(\mathbf{APS} + \underline{\mathbf{b}} \, \widehat{\underline{\Delta\mathbf{q}}}^T + \underline{\mathbf{T}} \, \widehat{\underline{\mathbf{v}}}^T \right)$$
$$= \underline{\mathbf{1}} \, \underline{\boldsymbol{\psi}}_m^T + \underline{\mathbf{E}}'' \tag{20}$$

where

- $\underline{\boldsymbol{\Psi}}[K \times H]$ contains the phases of the H PSs as seen by the K slave images;
- $\underline{\boldsymbol{\psi}}_m[H \times 1]$ contains the phases of the H PSs as seen by the master image, compensated for $\mathbf{APS}_{master}$;
- $\mathbf{APS}[K \times H]$ contains the estimated APS of each slave image;
- $\underline{\mathbf{E}}''[K \times H]$ is the residues matrix.

Consider now the following expression:

$$\gamma_h \triangleq \frac{1}{K} \sum_{k=1}^{K} \exp \left(j \underline{\boldsymbol{\zeta}}_{kh} \right). \tag{21}$$

It should be noted that the absolute value of γ_h ranges from 0 to 1 depending on the dispersion of the phases of the modified slave images with respect to the master. In correspondence of a PS, phase dispersion is low and $|\gamma_h|$ gets close to 1. Thus, $|\gamma_h|$ can be regarded as an *ensemble phase coherence*.

Apart from temporal decorrelation, phase stability is a function of the actual size of each scatterer within the imaged area. The effective dimension of the targets with respect to the resolution cell can be inferred analyzing the dispersion of the residual phases

$$\Gamma_k \triangleq \frac{1}{H} \sum_{h=1}^{H} \exp \left(j \underline{\boldsymbol{\zeta}}_{kh} \right) \tag{22}$$

as a function of the baseline (Appendix B). As will be shown, in correspondence of the PS grid, $|\Gamma_k|$ values are only slightly affected by the normal baseline.

F. PS Identification by Means of Phase Stability Analysis

So far, LOS velocity and DEM errors have been estimated for H image pixels selected by means of the amplitude dispersion index $D_{\mathcal{A}}$. However, due to the limits of the method for PSC selection, a number of PSs could have been neglected. PS identification can now be carried out by means of a time series analysis of the phase values.

In fact, once the APSs have been estimated and resampled on the uniform image grid, data can be compensated for this unwelcome phase contribution. After APS estimation and removal, we can finally compute DEM errors $\underline{\Delta\mathbf{q}}$ and target velocity $\underline{\mathbf{v}}$ on a pixel-by-pixel basis: small phase residues $\underline{\mathbf{E}}''$ with respect to the model will show the presence of further PSs.

To this end, we can use a simple periodogram, albeit with an irregular sampling of the two dimensions, baselines and time

$$\arg \max_{\Delta q, v} \left\{ |\gamma| = \left| \frac{1}{K} \sum_{k=1}^{K} e^{j\varphi_k} \cdot e^{-j(C_q B_k \cdot \Delta q + C_v T_k \cdot v)} \right| \right\} \tag{23}$$

where φ_k is the phase value of differential interferogram k relative to the generic image pixel after APS removal, $C_q = 4\pi/\lambda R \sin \alpha$ and $C_v = 4\pi/\lambda$. Basically, the unknowns v and Δq are estimated *maximizing the phase coherence γ of each image pixel*. The accuracy of the estimates depends on the geometrical and temporal baseline distribution and the phase stability of the target. For high SNR the following expressions hold [33]:

$$\sigma_{\Delta q}^2 \simeq \frac{\sigma_\varphi^2}{C_q^2 \sum (B_k - \overline{B})^2} \tag{24}$$

$$\sigma_v^2 \simeq \frac{\sigma_\varphi^2}{C_v^2 \sum (T_k - \overline{T})^2} \tag{25}$$

where σ_φ^2 is the phase noise variance (supposed independent of the acquisition), and $\overline{B}$ and $\overline{T}$ are the mean values of the geometrical and temporal baselines. Considering $\sigma_\varphi = 1$ and the baseline distribution of the ERS data set described in the experimental section, we get $\sigma_{\Delta q} \simeq 0.5$ m and $\sigma_v \simeq 0.5$ mm/yr. In fact, the expected elevation accuracy of the PS is, as usual, proportional to the baseline that in this case can be even larger than the decorrelation one. Referring to the actual ERS data base, baselines as large as 1600 m can usually be found and exploited.

The experiment carried out on the urban area of Ancona, Italy, described in the next section, shows that many PS are smaller than the resolution cell since the average value of the phase coherence $|\Gamma|$ does not decrease with the baseline as fast as it should in case of distributed scatterers (Appendix B). Therefore, a reasonable hypothesis to be confirmed by electromagnetic inversion studies is that, in the urban case, the PS are railings, corners (or equivalent) of buildings in reinforced concrete, etc. visible to the radar. In this case, the 1600 m baseline can be coherently exploited to get an elevation of ambiguity of about 5.5 m and thus elevation accuracies in the order of 50 cm, taking advantage of all the available data. Similar considerations hold for the estimated velocity field, but the accuracy will depend also on the agreement to the constant-velocity model.
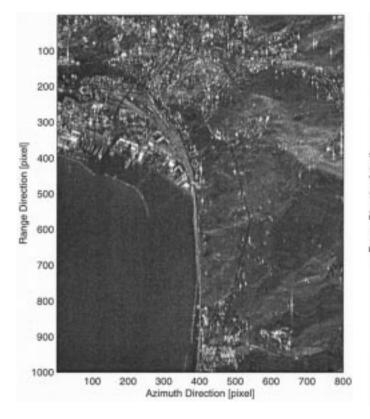
Fig. 2. Ancona, Italy: multi-image reflectivity map obtained using 34 ERS SAR acquisitions. Images were interpolated by a factor of four in range direction.
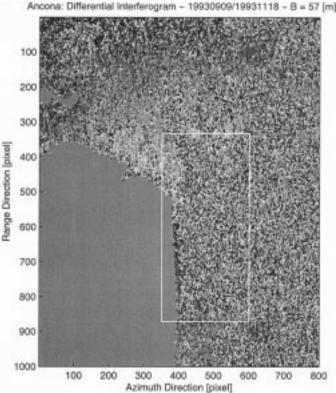

Fig. 3. Example of a differential interferogram over Ancona, Italy. Temporal baseline is 70 days (images were acquired on September 9 and November 18, 1993). Estimated normal baseline is 57 m. The area of interest, affected by terrain motion, corresponds to the low coherence area inside the white rectangle.

IV. EXPERIMENTAL RESULTS

The test area is a region about 5×4 km-wide in the Marche region (Eastern part of Central Italy). The area of the town of Ancona (Fig. 2) is of high geophysical interest because it is known to be very unstable. The big Ancona landslide of December 13, 1982 caused damages estimated at one billion U.S. dollars. The area is now periodically monitored and it is still subject to very slow terrain motion (< 1 cm/yr). Since the area is strongly affected by temporal decorrelation (Fig. 3), the analysis was carried out in a multi-image framework. 34 ERS SAR images gathered over the city (with a maximum relative temporal baseline of more than five years and a maximum relative normal baseline of more than 1600 m) were co-registered on a unique master (ERS-2 orbit 13 460 taken on November 16, 1997). The local DEM was estimated starting from six tandem pairs using the wavelet technique described in [2]. After DEM compensation, 33 differential interferograms were generated.

In order to select the PSC subset, a map of the amplitude dispersion index was computed, starting from the 34 amplitude images of the data set corrected for the different calibration factors $\mathcal{K}_k$ (Fig. 4). Analysis of this map shows interesting features. In particular, it should be noted that sea pixels and vegetated areas are characterized by high $D_{\mathcal{A}}$ values (> 0.5), corresponding to fully developed speckle statistics (Rayleigh distribution) or strong changes of the backscattering coefficient (e.g., due to Bragg reflections over the sea). On the other hand, several pixels

characterized by low $D_{\mathcal{A}}$ values (black spots) can be identified. Values as low as 0.11 have been estimated. About 500 targets with $D_{\mathcal{A}} < 0.25$ were selected as PSC.

On the PSC sparse grid, we carried out a joint estimation of DEM errors (with respect to that obtained from the six tandem pairs included in the data set), LOS velocities, and linear APS contributions, as described in the previous section of this paper. Solving the nonlinear system 13, by means of the iterative algorithm described in Appendix B, turned out to be very fast, since convergence was reached after a few iterations (~ 10).

Atmospheric phase contributions was then estimated and resampled on the uniform image grid by kriging interpolation [35]. All differential interferograms were then compensated for the estimated atmospheric contribution. In Fig. 5, an example of APS relative to the August 1996 ERS2 acquisition is reported. A joint estimation of both DEM errors and target velocity was then carried out on a pixel-by-pixel basis. PSs are characterized by low phase residues (high ensemble coherence values: $|\gamma_h| > 0.75$). We finally obtained that about 1% of the image pixels can be exploited for reliable phase measurements.

Fig. 6 shows the phase coherence map (23) of the data. Areas suffering temporal decorrelation look black, whereas stable targets are easily identified. Two considerations are in order. First, PS density in urban areas can be very high, allowing very accurate spatial sampling (> 100 PS/km² [4]). Nevertheless, not *all* the buildings can be monitored by means of this technique. Next, a comparison between Figs. 6 and 4 shows that dispersion
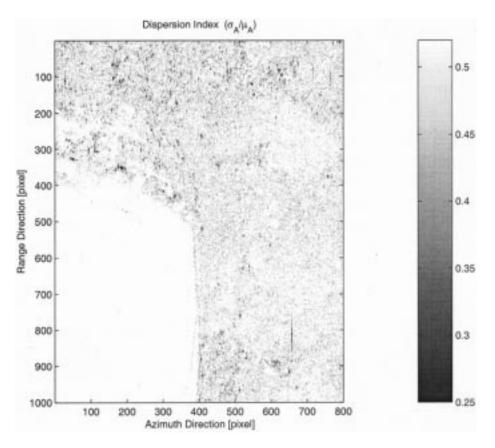
Fig. 4.   Amplitude dispersion index (D_A) of the 34 ERS SAR images of the Ancona data set computed on a pixel-by-pixel basis. It should be noted that sea pixels exhibit vey high relative dispersions ($D_A > 0.5$). On the contrary, black spots correspond to stable targets, characterized by low amplitude dispersions ($D_A < 0.25$). In the area under study, about 500 PS candidates were identified. Though values as low as 0.11 have been computed, the gray level scale has been limited for visualization purposes.
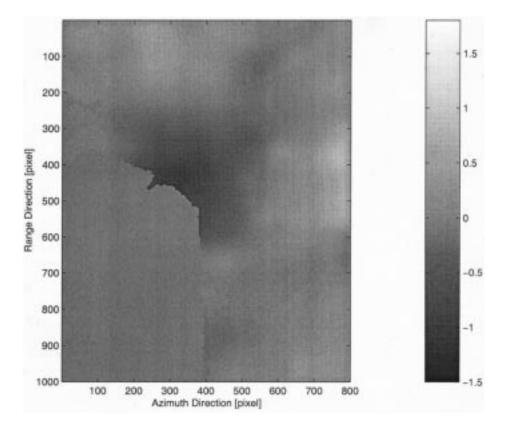

Fig. 5.   Estimated atmospheric phase screen (on land pixels) relative to the ERS2 SAR image acquired on August 18, 1996. Values are given in radians.

Fig. 6.   Phase coherence map after APS removal and compensation for target velocity and elevation error.
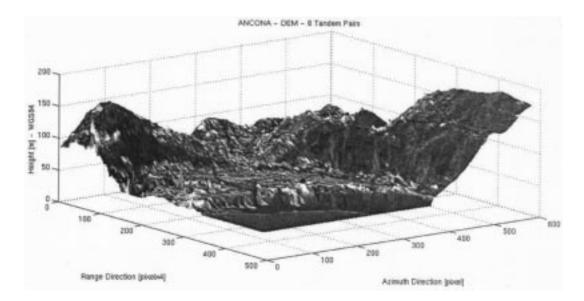

Fig. 7.   Ancona: perspective view of the harbor. The DEM was estimated combining six tandem interferograms. For visualization purposes, the vertical axis has been magnified.

index thresholding is not enough for detecting all the PS and it is worth carrying out all the processing steps.

After DEM correction, PSs location is known to a fraction of meter depending on the local SNR. In Figs. 7 and 8, a comparison between the DEM obtained combining six tandem pairs and the improved DEM estimated using all the data is shown (for visualization purposes the vertical scale has been magnified). Of course, DEM was improved only where PSs were identified. The multi-interferogram approach strongly reduces the impact of phase noise and residual atmospheric effects both on DEM errors and motion estimation. In Fig. 9, the map of the PSs affected by linear motion is reported. As already mentioned, the sliding area is subject to very slow terrain motion. Nevertheless, it can be monitored with a high degree of accuracy. An example of a time series of the differential phase values corresponding to a target in the sliding area is reported in Fig. 10. After APS removal, the accuracy of the velocity estimation of a PS can be lower than 1 mm/yr depending on the
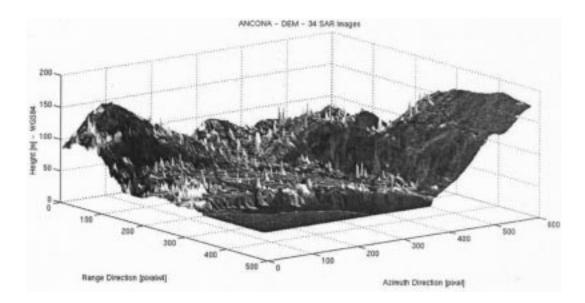
Fig. 8.   Ancona: Three-dimensional (3-D) perspective view of the harbor. The local DEM was optimized on the PSs using all the 34 SAR images available. PSs elevation error is now less than 1 m.
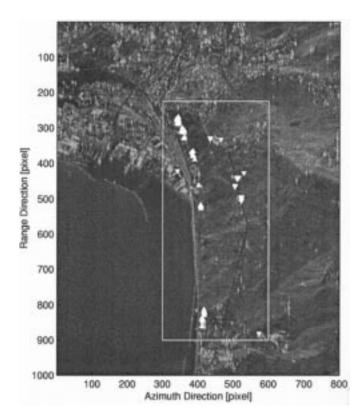

Fig. 9.   Multi-image reflectivity map of the Ancona area: target affected by significant linear motion have been highlighted. In the image, "up-triangles"' correspond to PSs with positive LOS velocity greater than 3 mm/yr, and "down-triangles" correspond to PSs with LOS subsidence rate greater than 3 mm/yr. For the sake of clarity, stable PSs (about 1000 targets with phase coherence greater than 0.9 and zero LOS velocity) have not been reported.

Fig. 10.   Example of time series relative to a PS in the sliding area of Ancona. Estimated velocity is 5±0.4 mm/yr (after APS removal).

number of acquisitions, the PSs density (for APS estimation), and temporal baselines dispersion. Comparison of the final velocity field with ground truth (optical leveling) relative to previous ground surveys over Ancona sliding area confirmed the reliability of the results [31].
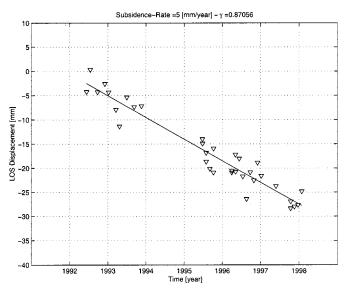
Finally, in order to get an estimation of the PS size, the dispersion of the residual phase values in correspondence with the PS (22) of each slave image has been computed as a function of the normal baseline. Results (Fig. 11) show a very weak dependance of $|\Gamma_h|$ on the look angle. Fitting the data with equation (36), the estimated PS size in range direction turned out to be about 0.25 of the resolution cell. The decorrelation rate is lower than what we measured for a rocky area on the Etna volcano in Sicily [7], confirming that, especially in urban areas, most of the PSs correspond to almost pointwise targets.

V. CONCLUSIONS

We have shown that in urban areas and in rocky terrain, PSs exist that allow us to extract useful phase information on a sparse
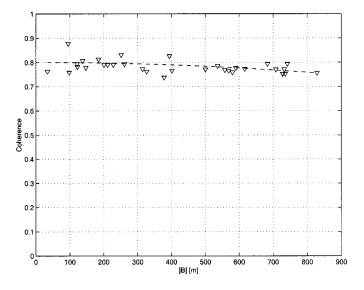
Fig. 11. Ancona data set: coherence Γ versus absolute value of normal baseline. The dashed line corresponds to (36) with $\Delta = 2$ m. PSs in urban areas exhibit almost no geometrical decorrelation due to their small dimensions with respect to the resolution cell.

grid of targets even if the time lapse between the takes is many years long. The spatial dimensions of the scatterers can be selected to be small with respect to the range resolution so that baselines longer than the critical one can be used. The PS density was seen to be sufficient (at least in towns and on rocky terrain [7]) to allow an estimation the atmospheric disturbance (the APS) with a sufficient spatial resolution. APS removal can then be performed, and a better estimation of both local topography and terrain deformation can be carried out.

The use of all the data of the ERS data set relative to the area of interest allows one to estimate long-term pixel motion with an accuracy that was previously attainable using optical techniques only. The data base of the PSs locations that can be created using ERS data could be used with other platforms, partially compensating low orbit stability that may produce excessive baselines. Other applications might be the use of the pointwise character of the PS to bridge the frequency change between ERS and ENVISAT or maybe even the angle change with RADARSAT, etc. The synergistic use of more platforms could in turn improve the revisiting times, bringing the interferometric tool to an operational stage even during seismic or volcanic crises. It will be interesting to check whether the phase measurements on the sparse grid of the PS could be used to improve the positioning of the satellite. Sure enough, the PS density may prove to be too low in vegetated areas so that artificial PS, namely, corner reflectors (CRs), will have to be added in some locations. However, first tests indicate that rather small CRs, with approximately a 1500 m^2 cross section, should suffice.

Several questions remain to be studied, such as the following. What is the distribution of PSs in different types of terrain? What is the possibility of reducing the threshold coherence level to extend their number? What is the physical nature of the PSs in towns and on rocky terrain, etc.? What is the quality of the APS estimates and their statistics?

The use of PS appears very promising in town subsidence studies to analyze small and slow motion of buildings trying

to detect collapse precursors and for volcanic up-swelling studies. Another application that should be feasible could be the daily measurement of pre seismic motions on entire cities using bistatic radar in connection with quasi-geostationary illuminators [32].

APPENDIX A
ALGORITHM FOR LINEAR APS CONTRIBUTIONS ESTIMATION

Let us consider a relatively small area on the ground and let us suppose that H PS candidates have been selected and their motion is almost completely described by a pixel-dependent but time-constant velocity. The nonlinear system 13 can be solved iteratively using the following algorithm:

1. $\bullet$ Let n be the iteration counter (starting from $n = 0$) and let

$$\underline{\Delta\Phi}^{(0)} = \underline{\Delta\Phi} \quad \underline{\Delta q}^{(0)} = \underline{\delta q}^{(0)} = \underline{v}^{(0)} = \underline{\delta v}^{(0)} = \underline{0}.$$

$\bullet$ Repeat until convergence:

(a) Update iteration counter and unknown vectors $\underline{v}$ and $\underline{\Delta q}$:

$$n = n + 1$$
$$\underline{\Delta q}^{(n)} = \underline{\Delta q}^{(n-1)} + \underline{\delta q}^{(n-1)}$$
$$\underline{v}^{(n)} = \underline{v}^{(n-1)} + \underline{\delta v}^{(n-1)}.$$

(b) If the following conditions are satisfied:

$$n > 1 \quad \left\|\underline{\Delta q}^{(n)} - \underline{\Delta q}^{(n-1)}\right\|_{L^\infty} < T_q$$
$$\left\|\underline{v}^{(n)} - \underline{v}^{(n-1)}\right\|_{L^\infty} < T_v$$

or $n = N_{\mathrm{MAX}}$(where N_{MAX} is the maximum number of iterations, $\|\underline{x}\|_{L^\infty} = \max\{|\underline{x}|\}$ and T_q and T_v are suitable thresholds), exit the cycle.

(c) Compensate $\underline{\Delta\Phi}$ for phase contributions due to $\underline{\Delta q}^{(n)}$ and $\underline{v}^{(n)}$

$$\underline{\Delta\Phi}^{(n)} = \underline{\Delta\Phi} - \left(\underline{b}\cdot\underline{\Delta q}^{(n)^T} + \underline{\mathbf{T}}\,\underline{v}^{(n)^T}\right). \quad (26)$$

(d) For each row k of $\underline{\Delta\Phi}^{(n)}$, estimate $\{a_k^{(n)}, p_{\xi k}^{(n)}, p_{\eta k}^{(n)}\}$ using a periodogram

$$\left\{p_{\xi k}^{(n)}, p_{\eta k}^{(n)}\right\} = \arg \max_{p_{\xi k}, p_{\eta k}} \left\{\left|\Gamma_k^{(n)}\left(p_{\xi k}, p_{\eta k}\right)\right|\right\}$$
$$a_k^{(n)} = \measuredangle\Gamma_k^{(n)} \quad (27)$$

where

$$\Gamma_k^{(n)} = \frac{1}{H}\sum_{h=1}^{H} e^{j\Delta\Phi_{kh}^{(n)}} \cdot e^{-j(p_{\xi k}\xi_h + p_{\eta k}\eta_h)}. \quad (28)$$

(e) Compensate the data for the estimated linear phase contributions

$$\underline{\Delta\Phi}^{(n-NoPlane)}$$
$$= \underline{\Delta\Phi}^{(n)} - \left(\underline{a}^{(n)}\underline{1}^T + \underline{p}_\xi^{(n)}\,\underline{\xi}^T + \underline{p}_\eta^{(n)}\underline{\eta}^T\right). \quad (29)$$

(f) For each PSC h (i.e., for each column of $\underline{\Delta\Phi}^{(n-NoPlane)}$), estimate the residual velocity and DEM error $\{\delta q_h, \delta v_h\}$, weighting each datum with the absolute value of Γ_k

$$\{\delta q_h^{(n)}, \delta v_h^{(n)}\} = \arg \max_{\Delta q_h, v_h} \{|\gamma_h(\delta q_h, \delta v_h)|\} \qquad (30)$$

with

$$\gamma_h = \frac{1}{K} \sum_{k=1}^{K} \left|\Gamma_k^{(n)}\right| \cdot e^{j\underline{\Delta\Phi}_{kh}^{(n-NoPlane)}}$$

$$\cdot e^{-j(C_q B_k \cdot \delta q + C_v T_k \cdot \delta v)}\} \qquad (31)$$

where $C_q = 4\pi/\lambda R \sin\alpha$, and $C_v = 4\pi/\lambda$.

Basically, DEM errors $\underline{\Delta q}$ and velocities $\underline{v}$ are computed starting from small spatial and temporal baselines (the only ones giving rise to high values of $|\Gamma_k|$ during the first iterations) and improve their accuracy as soon as better estimation and removal of the linear phase terms ($\underline{a}$, $\underline{p}_\xi$, $\underline{p}_\eta$) have been carried out. Provided that conditions outlined in Section III are satisfied, convergence is usually very fast ($\sim$10 iterations with $\sim$500 PSC and $\sim$30 images).

APPENDIX B
MEASURING THE PS DIMENSION

In this Appendix, we discuss how to estimate the "electromagnetic width" of each PS from its residual phase dispersion as a function of the baseline after APS removal. To get simple formulas, we shall make an approximation, namely, that we have many independent scatterers in the resolution cell and that terrain slopes (in azimuth and range) are constant within the resolution cell. Let g_i be the reflectivity modulus of a single scatterer within the cell and ϕ_i its interferometric phase

$$\phi_i = \frac{4\pi}{\lambda R \tan\alpha} B \cdot \eta_i = k \cdot \eta_i; \qquad k = \frac{4\pi}{\lambda R \tan\alpha} B \quad (32)$$

where

η_i scatterer slant range position;
α local incidence angle;
B normal baseline.

Then the following coherence expression holds:

$$\gamma = E \left[\frac{\left|\sum_i g_i^2 e^{j\phi_i}\right|}{\sum_i g_i^2} \right]. \qquad (33)$$

If we approximate the ratio of the sums with the ratio of the expected values, and if we accept the independence of reflectivity g_i, we get

$$\gamma \simeq E \left[\frac{E\left[g^2\right] \left|E\left[e^{jk\eta}\right]\right|}{E\left[g^2\right]} \right] = \left|E\left[e^{jk\eta}\right]\right|. \qquad (34)$$

Moreover, if $p(\eta)$ is the probability density of the scatterer slant range position, we can write

$$\gamma = \left|\int p(\eta) e^{jk\eta} d\eta\right| = |P(k)| \qquad (35)$$

where $P(k)$ is the Fourier transform of $p(\eta)$. In the case of a uniform scatterers distribution in the interval $\pm\Delta/2$ (Δ being the slant range resolution cell), we get

$$\gamma = \left|\frac{\sin(k\Delta/2)}{k\Delta/2}\right|. \qquad (36)$$

The first zeros of γ are in $k = \pm(2\pi/\Delta)$ or, using the expression of k in (32) in correspondence of the decorrelation baseline

$$B = \pm\frac{\lambda R \tan\alpha}{2\Delta} \simeq \pm 1100 \text{ m for flat terrain in the ERS case.}$$

On the other hand, if the scatterers are not uniformly distributed along the resolution cell but we have scatterers with a dominant backscattering coefficient concentrated in a smaller area, we get a larger decorrelation baseline. As a limit, dominant pointwise scatterers would be coherent with unlimited baselines (pointwise targets). If we know where these PSs are located, then we can illuminate them with any other SAR of comparable resolution. On these pointwise PSs, we would get interferometry notwithstanding rather unstable platforms, and this could lead to improved revisit times.

REFERENCES

[1] A. Ferretti, A. Monti Guarnieri, C. Prati, and F. Rocca, "Multi-baseline interferometric techniques and applications," in *Proc. FRINGE '96 Workshop*, Zurich, Switzerland, 1996.
[2] A. Ferretti, C. Prati, and F. Rocca, "Multibaseline InSAR DEM reconstruction: The wavelet approach," *IEEE Trans. Geosci. Remote Sensing*, vol. 37, pp. 705–715, Mar. 1999.
[3] ——, "Permanent scatterers in SAR interferometry," in *Proc. Int. Geosci. Remote Sensing Symp.*, Hamburg, Germany, June 28–July 2 1999, pp. 1528–1530.
[4] ——, "Non-linear subsidence rate estimation using permanent scatterers in differential SAR interferometry," *IEEE Trans. Geosci. Remote Sensing*, vol. 38, pp. 2202–2212, Sept. 2000.
[5] A. Ferretti, C. Prati, F. Rocca, and A. Monti Guarnieri, "Multi-baseline SAR interferometry for automatic DEM reconstruction," in *Proc. 3rd ERS Symp.*, Florence, Italy, 1997.
[6] C. Prati, F. Rocca, A. Monti Guarnieri, and P. Pasquali, "Interferometric techniques and applications," ESA Study Contract Rep. Contract N.3-7439/92/HGE-I, Ispra, Italy, 1994.
[7] A. Ferretti, C. Prati, and F. Rocca, "ESA empedocle project: Monitoring mount etna by space techniques-POLIMI SAR group-final report," ESA Study Contract Rep. Contract N. 13 155/98/I-DC, Ispra, Italy, 1999.

[8] H. A. Zebker and P. Rosen, "Atmospheric artifacts in interferometric SAR surface deformation and topographic maps," *J. Geophys. Res. Solid Earth*, vol. 102, no. B4, pp. 7547–7563, 1997.

[9] H. A. Zebker and R. Goldstein, "Topographic mapping from SAR observation," *J. Geophys. Res.*, vol. 91, no. B5, pp. 4993–4999, 1986.

[10] H. A. Zebker and J. Villasenor, "Decorrelation in interferometric radar echoes," *IEEE Trans. Geosci. Remote Sensing*, vol. 30, pp. 950–959, Sept. 1992.

[11] R. Goldstein, "Atmospheric limitations to repeat-pass interferometry," *Geophys. Res. Lett.*, vol. 22, pp. 2517–2520, Sept. 1995.

[12] A. K. Gabriel, R. M. Goldstein, and H. A. Zebker, "Mapping small elevation changes over large areas: differential radar interferometry," *J. Geophys. Res.*, vol. 94, no. B7, pp. 9183–9191, July 1989.

[13] H. Laur, P. Bally, P. Meadows, J. Sanchez, B. Schaettler, E. Lopinto, and D. Esteban, "Derivation of the backscattering coefficient sigma-nought in ESA ERS SAR PRI," ESA Document No: ES-TN-RS-PM-HL09, http://earth.esa.int/esc_intro.htm, Ispra, Italy, Sept. 1998.

[14] C. Prati, F. Rocca, A. Monti Guarnieri, and E. Damonti, "Seismic migration for SAR focusing: Interferometrical applications," *IEEE Trans. Geosci. Remote Sens.*, vol. 28, pp. 627–640, July 1990.

[15] T. Dixon, Ed., "SAR Interferometry and Surface Change Detection," Rep. Workshop, Boulder, CO, http://southport.jpl.nasa.gov/scienceapps/dixon/index.html, Feb. 1994.

[16] D. Massonnet *et al.*, "The displacement field of the landers earthquake mapped by radar interferometry," *Nature*, vol. 364, pp. 138–142, July 8, 1993.

[17] D. Massonnet and A. Arnaud, "Deflation of Mount Etna monitored by space radar interferometry," *Nature*, vol. 375, pp. 567–570, 1995.

[18] A. Papoulis, *Probability, Random Variables, and Stochastic Processes*. New York: McGraw-Hill, 1984.

[19] H. L. Van Trees, *Detection, Estimation, and Modulation Theory*: Wiley, 1968.

[20] C. Prati, F. Rocca, and A. Monti Guarnieri, "SAR interferometry experiments with ERS-1," in *Proc. 1st ERS-1 Symp.*, Cannes, France, Nov. 4–6, 1992, pp. 211–218.

[21] M. Costantini and P. Rosen, "A generalized phase unwrapping approach for sparse data," in *Proc. Int. Geosci. Remote Sensing Symp.*, Hamburg, Germany, June 28–July 2 1999, pp. 267–269.

[22] M. Eineder and J. Holzner, "Phase unwrapping of low coherence differential interferograms," in *Proc. Int. Geosci. Remote Sensing Symp.*, Hamburg, June 28–July 2 1999, pp. 1727–1730.

[23] C. Werner, S. Hensley, R. M. Goldstein, P. A. Rosen, and H. A. Zebker, "Techniques and applications of SAR interferometry for ERS-1: Topographic mapping, change detection, and slope measurement," in *Proc. First ERS-1 Symp.*, Cannes, France, Nov. 4–6 1992, pp. 205–210.

[24] S. Williams, Y. Bock, and P. Pang, "Integrated satellite interferometry: Tropospheric noise, GPS estimates and implications for interferometric synthetic aperture radar products," *J. Geophys. Res.*, vol. 103, no. B11, pp. 27 051–27 067, 1998.

[25] E. Rodriguez and J. M. Martin, "Theory and design of interferometric synthetic aperture radars," *Proc. Inst. Elect. Eng. F*, vol. 139, pp. 147–159, Apr. 1992.

[26] R. Hanssen, "Assessment of the role of atmospheric heterogeneities in ERS tandem SAR interferometry," DEOS Report 12 698.1, Delft Univ., Delft, The Netherlands, 1998.

[27] R. Bamler and D. Just, "Phase statistics and decorrelation in SAR interferograms," in *Proc. Int. Geosci. Remote Sensing Symp.*, Tokyo, Japan, August 18–21 1993, pp. 980–984.

[28] C. Carnec, ""Interferometrie SAR differentielle," Application à la detection des mouvements du terrain," Ph.D. dissertation, Univ. Paris 7, Paris, France, 1996.

[29] R. Scharroo, P. N. A. M. Visser, and G. J. Mets, "Precise orbit determination and gravity field improvement for ERS satellites," *J. Geophys. Res.*, vol. 103, no. C4, pp. 8113–8127, 1998.

[30] C. Reigber, Y. Xia, H. Kaufmann, T. Timmen, J. Bodechtel, and M. Frei, "Impact of precise orbits on SAR interferometry," in *Proc. FRINGE 96 Workshop*, Zurich, Switzerland, 1996.

[31] A. Mazzotti, private communication.

[32] C. Prati, F. Rocca, D. Giancola, and A. Monti Guarnieri, "Passive geosynchronous SAR system reusing backscattered digital audio broadcasting signals," *IEEE Trans. Geosci. Remote Sensing*, vol. 36, pp. 1973–1976, Nov. 1998.

[33] D. C. Rife and R. R. Boorstyn, "Single-tone parameter estimation from discrete-time observations," *IEEE Trans. Inform. Theory*, vol. IT-20, pp. 591–598, Sep. 1974.

[34] S. Usai and R. Klees, "On the feasibility of long time scale INSAR," in *Proc. Int. Geosci. Remote Sensing Symp.*, Seattle, WA, July 6–10 1998, pp. 2448–2450.

[35] H. Wackernagel, *Multivariate Geostatistics*, 2nd ed. Berlin, Germany: Springer-Verlag, 1998.

Alessandro Ferretti was born in Milano, Italy, on January 27, 1968. He received the "Laurea" and Ph.D. degrees in electrical engineering from the Politecnico di Milano (POLIMI) in 1993 and 1997, respectively, writing his thesis on the use of multibaseline SAR interferograms for more reliable phase unwrapping algorithms, and the Master degree in information technology from Politecnico (private firms consortium) CEFRIEL, in 1993, working on digital audio compression (psychoacoustic applications to source coding algorithms).

In May 1994, he joined the POLIMI SAR group working on SAR interferometry and digital elevation model reconstruction. In the summer of 1996, he was with the Department of Geomatic Engineering (formerly Photogrammetry and Surveying), University College London, London, U.K. His research interests are in digital signal processing and remote sensing. He is Managing Director of the company "Tele-Rilevamento Europa—T.r.E.," a commercial spin-off of Politecnico di Milano.

Claudio Prati was born in Milano, Italy, on March 20, 1958. He received the "Laurea" degree in electronic engineering in 1983 and the Ph.D. degree in 1987, both from the Politecnico di Milano (POLIMI).

In 1987, he joined the Centro Studi Telecomunicazioni Spaziali of the National Research Counci, Milano. He was with Department of Geophysics of Stanford University as a Visiting Scholar during the Fall of 1987. Since 1991, he has been Associate Professor of systems for remote sensing, POLIMI. He has been the external responsible for the interferometric experiments with the European Microwave Signature Laboratory, Joint Research Center, Ispra, Italy. His main research interests are in digital signal processing in noise suppression, emission tomography, and synthetic aperture radar (SAR), where he has studied new focusing techniques and interferometrical applications of SAR data. He has written more than 50 papers on these topics.

Prof. Prati received the IEEE Geoscience and Remote Sensing Society 1989 Symposium Prize Paper award. He holds, with Prof. F. Rocca, a U.S. Patent (5 332 999, July 26, 1994) on a "Process for generating Synthetic Aperture Radar Interferograms."

Fabio Rocca received the Dottore in ingegneria elettronica from the Politecnico di Milano (POLIMI), in 1962.

He has worked in the Department of Electronic Engineering, POLIMI, where he is currently Professor of Digital Signal Processing. His research activities in seismics were dedicated to multichannel filtering, interpolation of faulted surfaces, migration in the frequency domain, dip moveout processing, nonlinear deconvolution, offset and shot continuation, and recently, the use of drill bit noise for "while-drilling" investigations. His nonseismic research activities have been dedicated to television bandwidth compression, where he introduced and analyzed the technique of motion compensation in emission tomography and in synthetic aperture radar (SAR). From 1982 to 1983, he was President of the Osservatorio Geofisico Sperimentale, Trieste, Italy, where he is now Coordinator of the Scientific Council. He is a member of the Scientific Council of the Institut Français du Pétrole, Paris, France.

Dr. Rocca is a Past President and Honorary Member of the European Association of Exploration Geophysicists and an Honorary Member of the Society of Exploration Geophysicists. He was awarded the Honeywell International Award (HUSPI) for biomedical image processing applications in 1979, the Symposium Prize Paper Award at the IGARSS 89 and the 1990 Schlumberger Award of the EAGE and the Italgas Award for Telecommunications in 1995.